Sensors and Actuators A 316 (2020) 112269

Contents lists available at ScienceDirect

Sensors and Actuators A: Physical

journal homepage: www.elsevier.com/locate/sna

Magnetoelectric wireless power transfer for biomedical implants: Effects of non-uniform magnetic field, alignment and orientation

Binh Duc Truong, Erik Andersen, Curtis Casados, Shad Roundy

Department of Mechanical Engineering, University of Utah, Salt Lake, UT 84112, USA

ARTICLE INFO

Article history:
Received 11 May 2020
Received in revised form 16 July 2020
Accepted 6 August 2020
Available online 28 August 2020

Keywords:
Magnetoelectric transducer
Wireless power transfer
Non-Uniform magnetic field
Power optimization
Mis-alignment/orientation

ABSTRACT

This article presents experimental validation of a generalized equivalent two-port model for a magnetoelectric-based wireless power transfer system (WPTS) that utilizes a circular multi-turn coil as a transmitter, with a focus on potential application to biomedical implantable devices. The central objective of the work is to investigate the performance of the power delivered to a resistive load under uncertainties in magnetoelectric receiver position and orientation. In addition, the effects of a non-uniform applied magnetic field are considered. For the particular experimental system being studied, a maximum transferred power of 4.91 mW is obtained at a distance of 3 cm between the centers of the coil and the magnetoelectric (ME) transducer, in which the corresponding magnetic flux density is 225.8 μT. As the distance increases to 6 cm, the generated power drops to 1.97 mW. Furthermore, we find that the output power is proportional to the squared cosine of the misorientation angle, compared to the power achieved at the nominal (zero-angle) position. Meanwhile, as expected, the delivered power is less sensitive to misalignment since the width of the receiver is relatively small in comparison with the diameter of the transmit coil. In general, the power produced at the load is a quadratic function of the effective magnetic field that is projected onto the operating direction of the ME laminated composite (i.e., the longitudinal axis in this case). All findings are expected to provide a universal comprehensive picture of the dynamics and performance of the ME WPTS. The presented device concept could open an alternative pathway for powering implants.

© 2020 Elsevier B.V. All rights reserved.

1. Introduction

The Internet of Things (IoT) for healthcare has received worldwide research effort for many biomedical applications such as health monitoring and therapeutic treatment of dysfunctional organs. Healthcare activities based on wireless sensor networks provide secure transmission and reception of medical signals both for early diagnosis and for real-time observation of health status [1,2]. A well-known early implant is a cardiac pacemaker, which is installed in the heart through surgery to manage irregular rhythm, for instance, tachycardia (too fast) or bradycardia (too slow) [3]. In the last decades, the rapid progress of implantable medical devices (IMDs) has seen extraordinary growth to have functionality and packaging proper for biological implantations [4]. However, almost all IMDs so far have been powered by batteries that occupy the majority of space in an implanted system, posing a challenge to effort to miniaturize the entire implanted system. The battery has to be replaced or recharged regularly due to its limited lifetime. In order to increase the longevity of IMDs, efforts to power the implant by alternative contactless means has become more prevalent. Central to this ongoing advancement is wireless power transfer (WPT) [5]; a technology that offers not only long-term sustainability but also greater flexibility, reliability, and safety [6,7].

A wireless power transfer system (WPTS) enables the biomedical implant by wave transmission through the air and multi-layer tissue media. The WPT methods are generally categorized into two schemes, near-field and far-field, depending on the operating frequency and the transfer distance between the transmitter and receiver [8]. In lossy dielectrics (e.g., skin, fat, and muscle), the far-field waves suffer from significant path loss as a result of high energy absorption [9]. Furthermore, the higher frequency waves used in far-field transmission, resulting in higher energy absorption in human tissue, are potentially more harmful to the human body, and so are more tightly limited by standard regulations [10–13]. By contrast, near-field systems are more efficient (i.e., lower power dissipation) in lossy media [14], and therefore are generally more suitable for bio-implantable applications.

Two well-established methods using electromagnetic fields are inductive coupled resonators [15,16] and electrodynamic coupling

E-mail address: Binh.D.Truong@utah.edu (B.D. Truong).

https://doi.org/10.1016/j.sna.2020.112269
0924-4247/© 2020 Elsevier B.V. All rights reserved.

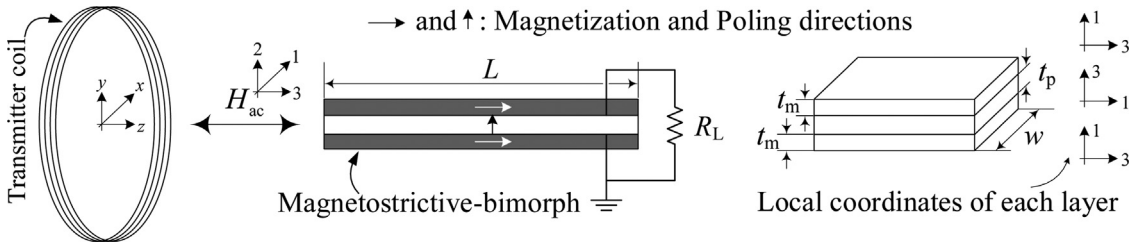

Fig. 1. Schematic of the WPTS utilizing a circular multi-turn coil as a transmitter and a magnetoelectric (ME) transducer as a receiver. The geometric dimensions of the ME laminated composite are included. (x, y, z) and $(1, 2, 3)$ are the global and local coordinates, respectively.

[17,18]. The latter is referred to here as the magneto-mechano-electric (MME) mechanism. Each technique has its own merits and drawbacks. The typical operating frequency of a resonant inductive coupling (RIC) system is in a range of MHz, which limits the maximum allowable magnetic flux density (**B**–field) that can be applied to humans. By contrast, MME devices operate at much lower frequencies which allow them to be exposed to much higher field strengths. For instance, the permissible **B**–field at 1 kHz is ∼300 μT, in comparison with 0.29 μT at 6.78 MHz, according to [12,13]. However, the weak coupling between the magnetic and mechanical domains of the MME resonator, which is realized by the interaction of a permanent magnet and the **B**–field, results in extremely low transmission efficiency. In order to overcome the limitations of those architectures, in this work, we introduce an alternative WPTS that utilizes a magnetoelectric (ME) transducer as a receiver. This approach manifests a higher coupling than MME structures and requires lower frequencies than RIC systems; therefore, it is possible to transfer energy into an implanted medical device more efficiently (than MME transducers) and at higher magnetic fields (than RIC) without violating the safety standards.

In practice, the position and orientation of IMDs cannot be perfectly controlled. Furthermore, it is almost impossible to generate a uniform **B**–field throughout the space from the transmitter to the receiver. Any variations in the receiver location may lead to a significant drop in the delivered power, making it insufficient for powering the IMDs. Thus, comprehending the effects of the field non-uniformity, device misalignment and misorientation is essential. These influences were thoroughly investigated for RIC and acoustic power transmission systems [19,20]. However, there has been no such a study on the ME WPTS in the literature. Addressing all of these concerns is the central objective of the article.

In a previous work [21], we presented in detail a two-port model for the receiver (a ME transducer), with an assumption that the external **B**–field is ideally uniform along the length of the laminated composite. To verify the model predictions, a Helmholtz coil was utilized as a transmitter, and the ME resonator was located at its center. In contrast, in this paper, the developed model is further generalized and validated for the case where a non-uniform magnetic field is employed. By making use of a circular multi-turn coil as a transmitter, the effects of the coil geometry on the distribution of the **B**–field now cannot be disregarded. Understanding the performance of a complete structure that takes into account the dynamics of both transmitting and receiving sides is important to design an optimal system and bridge the gap between ideal operation and realistic scenarios. With the aim to power low-power bioelectronics, we treat the actual transferred power as a key factor of the investigation, while leaving the transfer efficiency open for further consideration.

2. Device concept and Equivalent circuit model

Different from a RIC architecture, in which the magnetic energy is captured on the principle of Faraday's law of induction, a ME

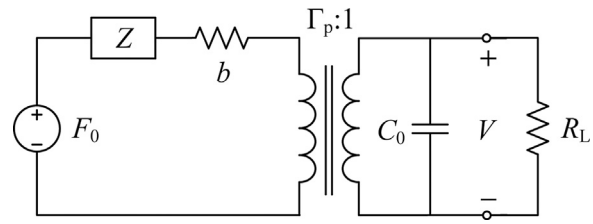

Fig. 2. Simplified equivalent circuit model for free-free ends configuration.

WPTS first converts the magnetic waves to mechanical vibrations through the interaction between the field and magnetostrictive material. The kinetic energy is then transformed into electrical energy at the final stage of conversion due to the piezoelectric effect. The overall ME coupling is dependent on not only the receiver geometry but also the intrinsic properties of materials in use. This characteristic could provide more degrees of freedom for transducer design and optimization in order to achieve a given desired power.

Fig. 1 shows the WPTS that is under consideration, in which a ME transducer is utilized as a receiver while a circular multi-turn coil is a transmitter. The ME laminate used for this study is composed of one PZT layer placed in between two Galfenol layers, bonded together by a conductive adhesive. The magnetostrictive material is magnetized in the length direction while the piezoelectric phase is poled in the thickness axis. The geometric dimensions of the ME generator are defined as in the figure; L, w, t_m and t_p are the beam length, width, and thicknesses of the two phases. (x, y, z) are the system global coordinates while the material local axes are denoted as $(1, 2, 3)$. The positive z–axis is coming out of the coil plane towards the ME laminate. The transmitter can be modeled as a thick coil that uses the current density instead of the current itself in order to eliminate the number of turns.

Under an external AC magnetic field (**H**–field) applied along the z–axis, a strain is induced inside the magnetostrictive material, which is then transferred to the piezoelectric layer through the bonding interfaces. As a consequence, the entire composite structure vibrates along the length direction, which is also the local axis 3 and 1 of the magnetostrictive and piezoelectric phases, respectively. Since the magnetization and polarization vectors are in parallel with the 3–direction, Galfenol and PZT operates in the longitudinal ($d_{33,m}$) and transversal ($d_{31,p}$) coupling. The power generation capability of the ME WPTS is evaluated by measuring the voltage across a resistor that is connected to the output terminals of the ME receiver.

The equivalent circuit model of the free-free configuration is shown in Figure 2, which was derived and experimentally validated in [21] under the condition that the applied magnetic flux density is uniform. Here, $F_0 = \Gamma_m H_0 \cos(\omega t)$ is the equivalent force input to the mechanical domain where Γ_m is the magneto-elastic transduction factor. The excitation magnetic field is sinusoidal with angular frequency ω, $H_{ac} = H_0 \cos(\omega t)$. We denote Z and b as the mechanical impedance and damping coefficient, respectively. Γ_p is the elec-

tromechanical transduction factor, C_0 is the nominal capacitance of the piezoelectric resonator, and V is the voltage generated on the resistor R_L.

The model parameters are given by

$$\Gamma_m = 2wt_m \frac{d_{33,m}}{s_{33}^H}, \tag{1}$$

$$Z = \frac{1}{2}\left(\frac{n}{s_{11}^E} + \frac{1-n}{\kappa s_{33}^H}\right)\frac{A}{j\bar{v}}\cot\left(\frac{\omega L}{2\bar{v}}\right), \tag{2}$$

$$\Gamma_p = -w\frac{d_{31,p}}{s_{11}^E}, \tag{3}$$

$$C_0 = \epsilon_{33}^S \frac{wL}{t_p} \tag{4}$$

where κ is the interface coupling coefficient representing the strain percentage transferred to the piezoelectric material from the magnetostrictive layers,

$$n = \frac{t_p}{t_p + 2t_m},\ 0 < n < 1, \tag{5}$$

$$A_1 = t_p w,\ A_2 = t_m w,\ A = (t_p + 2t_m)w, \tag{6}$$

$$\bar{v}^2 = \frac{1}{\bar{\rho}}\left[n\left(s_{11}^E - \frac{d_{31,p}^2}{\epsilon_{33}^T}\right)^{-1} + \frac{1-n}{\kappa}\left(s_{33}^H - \frac{d_{33,m}^2}{\mu_{33,m}^T}\right)^{-1}\right], \tag{7}$$

$$\bar{\rho} = \frac{\rho_p A_1 + 2\rho_m A_2/\kappa}{A_1 + 2A_2}. \tag{8}$$

The definitions of the material properties are as follows. ρ_p and ρ_m – mass densities of the piezoelectric and magnetostrictive phases, respectively. s_{11}^E – elastic compliance of the piezoelectric material under constant electric field. $d_{31,p}$ – transverse piezoelectric charge constant. ϵ_{33}^T – dielectric permittivity under constant stress. ϵ_{33}^S – permittivity component at constant strain with the plane-stress assumption of a thin narrow beam (i.e., $\epsilon_{33}^S = \epsilon_{33}^T - d_{31,p}^2/s_{11}^E$). s_{33}^H – elastic compliance of the magnetostrictive material at constant magnetic field. $d_{33,m}$ – piezomagnetic constant. $\mu_{33,m}^T$ – magnetic permeability at constant stress.

Based on the derivations presented in [21], the two-port model is now generalized for the case of a non-uniform external magnetic field and an arbitrary position of the ME receiver. The complex amplitude of the open-circuit voltage, $R_L \to +\infty$, is determined as

$$\hat{V}_\infty = \frac{\Gamma_p}{C_0}\frac{\Gamma_m\langle H_0\rangle}{j\omega(Z+b) + \Delta K} \tag{9}$$

where $\Delta K = \Gamma_p^2/C_0$ and $\langle H_0\rangle$ is the effective **H**–field amplitude. Denoting H_i as the projection of the total magnetic field acting on an infinitesimal mass element m_i onto the length direction of the laminated composite, $\langle H_0\rangle$ is then averaged over the entire volume of the magnetostrictive material,

$$\langle H_0\rangle = \frac{1}{N}\sum_{i=1}^{N} H_i \tag{10}$$

where N is the number of computational samples. The ME coefficient is defined by the rate of change of the open-circuit electric field $\hat{E}_{3,\infty}$ in response to the applied magnetic field $\hat{H}_3$,

$$\alpha_{ME} = \left|\frac{d\hat{E}_{3,\infty}}{d\hat{H}_3}\right| = \frac{\Gamma_p}{t_p C_0}\frac{\Gamma_m}{\sqrt{(\omega b)^2 + (\bar{Z} + \Delta K)^2}} \tag{11}$$

where the subscript {3} denotes the local coordinate of both piezoelectric and magnetostrictive phases, and $\bar{Z} = j\omega Z$ is a real function of the drive frequency ω,

$$\bar{Z} = \frac{1}{2}\left(\frac{n}{s_{11}^E} + \frac{1-n}{\kappa s_{33}^H}\right)\frac{A}{\bar{v}}\omega\cot\left(\frac{\omega L}{2\bar{v}}\right). \tag{12}$$

α_{ME} is independent of the applied magnetic field, but it is a function of operating frequency.

The power delivered to the load is derived as

$$P = \frac{1}{2}\frac{|\hat{V}|^2}{R_L} = \frac{1}{2}\Delta K\frac{\omega^2\tau}{1+(\omega\tau)^2}\Gamma_m^2\langle H_0^2\rangle \Big/ \left\{\left[\bar{Z} + \Delta K\frac{(\omega\tau)^2}{1+(\omega\tau)^2}\right]^2 + \left[\omega b + \Delta K\frac{\omega\tau}{1+(\omega\tau)^2}\right]^2\right\} \tag{13}$$

where $\tau = C_0 R_L$ is the electrical time constant, and

$$\langle H_0^2\rangle = \frac{1}{N}\sum_{i=1}^{N} H_i^2. \tag{14}$$

Validating equations (9), (11) and (13) are the main objectives of the article, taking into account the effects of non-uniform **H**–field, alignment and orientation.

3. Experimental validations

3.1. Experimental setup

Figure 3 shows the complete electrical setup to evaluate the output power of the ME WPTS. A single-coil, connected to an E&I 210L RF power amplifier, is used as a transmitter that generates a magnetic field as a means of power transmission. The receiver is a ME laminated composite, consisting of one PZT-5A and two TdVib Galfenol layers. The two materials are bonded together by EPO-TEK H20S, a conductive epoxy. Two rectangular K&J neodymium magnets are placed above and below the ME transducer to produce a DC magnetic field (as a bias) for its operation. The drive frequency and the power input to the transmitter are controlled by a Tektronix function generator. The output voltage is measured with a Tektronix 10 MΩ probe and collected by a Tektronix oscilloscope. In experiments, the average transferred power is determined by

$$P = \frac{1}{T}\int_0^T \frac{V^2(t)}{R_L}dt \tag{15}$$

where $V(t)$ is the waveform taken over a sampling period of time T. Under the open-circuit operation, $R_L \to +\infty$ and $P \to 0$. A 10–MΩ probe is used for approximating the open-circuit output voltage. All the model parameters are extracted from [21] and are listed in Table 1. This same set of constants is utilized to validate all following cases. The damping coefficient is computed from a damped harmonic oscillation of the measured open-circuit voltage. The interface coupling, which relates the strain transfer between the two phases (magnetostrictive and piezoelectric), is estimated by fitting the predicted anti-resonance frequency to its experimental value.

3.2. Open-circuit voltage and magnetoelectric coefficient

The ME coefficient, α_{ME}, is the most widely used factor for evaluating the performance of a ME transducer as it shows the direct relation between the induced electric field and the applied magnetic field. While α_{ME} is a material-oriented criterion, the open-circuit output voltage is the actual physical parameter that

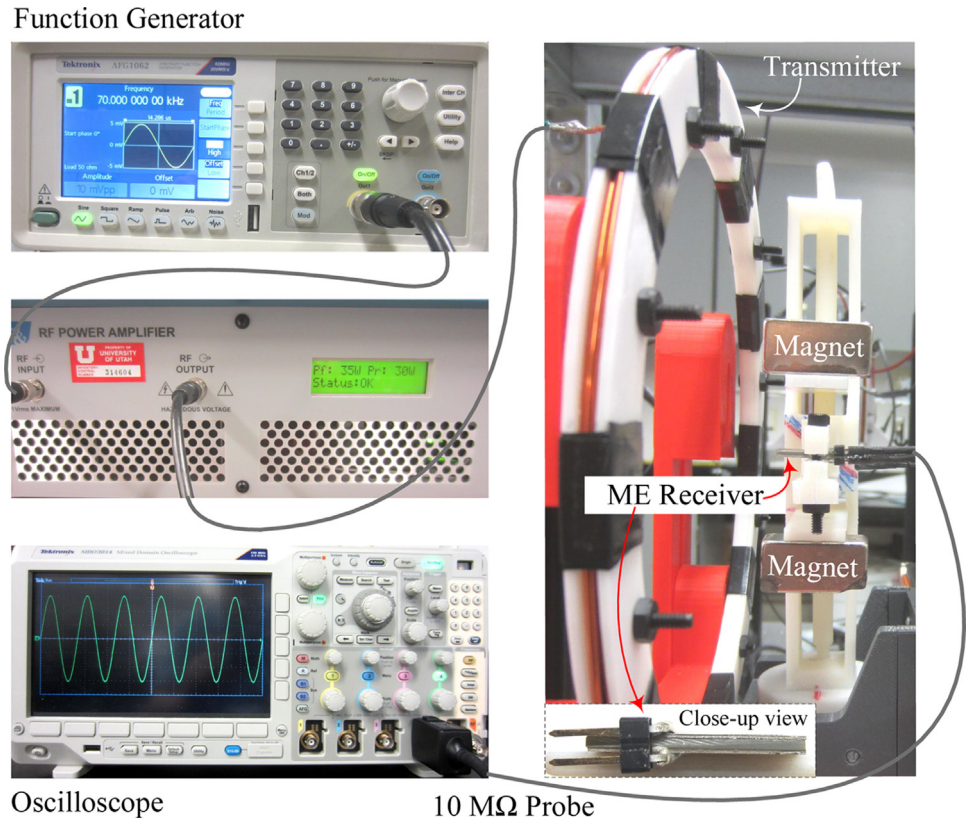

Fig. 3. Sketch of the electrical setup for measuring the power transferred to the load, including the experimental prototypes of the transmitting coil, the ME receiver and its close-up view.

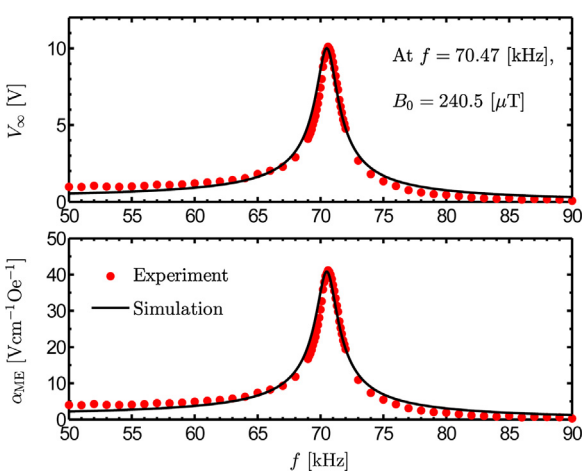

Fig. 4. Frequency responses of the open-circuit voltage V_∞ and the ME coefficient α_{ME}: Comparisons between the experimental data and simulation results. Unit conversion of magnetic field: 1 A/m = $4\pi \times 10^{-3}$ Oe.

magnetic field sensing applications concern. Therefore, it is worthwhile to investigate these aspects, although they are not the main aims of the work.

As proven in [18], operating an electromechanical-based WPTS at its anti-resonance frequency together with the corresponding optimal load is the most convenient method to approach the power transfer limit (i.e., the maximum power available at the mechanical domain). The anti-resonance frequency f_1, also known as the open-circuit resonance frequency, can be determined by considering the frequency responses of the open-circuit voltage amplitude V_∞ that are presented in Figure 4. A magnetic field sensor (model MC110A) is used to measure the **B**–field amplitude generated by the transmitter at $f = f_1$. The obtained results are $f_1 = 70.47$ kHz, $B_0 = 240.5$ μT and $\max\{V_\infty\} = 10.10$ V. Note that, the impedance of the transmit coil is a function of frequency. Hence, given the same source voltage, the input current decreases with respect to the increase of the operating frequency, which hence reduces the **B**–field strength. However, for the particular transmitter and frequency range in use, this effect can be neglected. In the simulations, the same value of B_0 is employed and V_∞ is calculated as $V_\infty = |\hat{V}_\infty|$ with $\hat{V}_\infty$ given in (9). The measured capacitance of the PZT layer is $C_0 = 2.95$ nF. A comparison between the experiments and predictions shows a good agreement. The frequency performance of the ME coefficient is included in the same figure, in which a $\max\{\alpha_{ME}\} = 41.17$ Vcm^{-1}Oe^{-1} is attained at the anti-resonance frequency.

In order to investigate the alteration of V_∞ over the change of the relative distance between the transmitter and receiver, we first use an analytical model of a thick coil to generate a map of the magnetic field strength along the coil centerline $(x, y, z) = (0, 0, z)$. The model is reliable for further studies as it was both numerically and experimentally validated [22,23]. This method relaxes the demand for the precise measurements of the **H**–field with a large number of sampling points (i.e., N in (10)) over a short distance range, which is challenging to implement due to the large size of the magnetic field sensor (MC110A). A summary of the theoretical formulation developed in [23] is presented in Appendix A.

Applying equation (18) for the transmitter and receiver geometries in Table 1, we find that, given the same z, the variation of the magnetic field in the longitudinal direction, $H_z(x, y, z)$, is negligible for $x^* \in [x - w/2, x + w/2]$ and $y^* \in [y - t/2, y + t/2]$ where $t = t_p + 2t_m$ is the total thickness of the ME laminate. In other words, $H_z(x^*, y^*, z) \approx H_z(x, y, z)$. Meanwhile, at the same x and y, the non-uniformity along the z–axis is more significant and cannot be neglected, $H_z(x, y, z^*) \neq H_z(x, y, z)$ for $z^* \in [z - L/2, z + L/2]$.

Table 1
Coil parameters, material properties and magnetoelectric transducer geometries.

Parameters	Value
Transmitter	
Inner radius, r_1	7.78, cm
Outer radius, r_2	8.35, cm
Lower height, z_1	−1.65, mm
Upper height, z_2	1.65, mm
Number of turns, N_c	9
Wire diameter, d_w	1.291, mm
PZT-5A4E	
Elastic constant, Y_{11}^E	66, GPa
Elastic compliance, s_{11}^E	$1/Y_{11}^E$, m^2/N
Piezoelectric constant, $d_{31,p}$	-190×10^{-12}, m/V
Dielectric permittivity, $\epsilon_{33}^T/\epsilon_0$	1800
Mass density, ρ_p	7800 kg/m^3
TdVib Galfenol	
Elastic constant, Y_{33}^H	40, GPa
Elastic compliance, s_{33}^H	$1/Y_{33}^H$, m^2/N
Piezomagnetic coefficient, $d_{33,m}$	7.77×10^{-9}, Wb/N
Magnetic permeability, $\mu_{33,m}^T/\mu_0$	100
Mass density, ρ_m	7800, kg/m^3
Receiver Geometry	
PZT thickness, t_p	1.02, mm
Galfenol thickness (each layer), t_m	370, μm
Total thickness, $t_0 = t_p + 2t_m$	1.76, mm
Laminated composite width, w	10, mm
Laminated composite length, L	20, mm
Mechanical characteristics	
Damping coefficient, b	4.22, Ns/m
Interface coupling, κ	62.2%

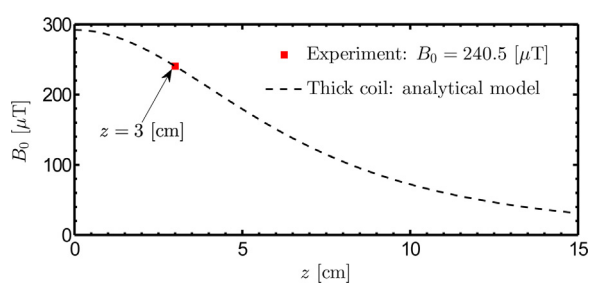

Fig. 5. Magnetic flux density amplitude B_0: Measured value at $z = 3$ cm and those obtained by the analytical model of a thick coil.

Therefore, for the sake of simplification, we only consider the change of the **H**–field with respect to z without compromising the final results.

Figure 5 shows the profile of the magnetic flux density strength along z. The current flowing into the transmitter coil (**I** in (18)) is adjusted, such that the simulation and experimental results of B_0 at $z = 3$ cm are identical. Figure 6 presents the influence of the non-uniform magnetic field on the open-circuit output voltage. The effective **H**–field amplitude $\langle H_0 \rangle$ is averaged over the length of the ME transducer with $N = 2000$, based on the prediction data obtained in Figure 5. The operating frequency is at the anti-resonance frequency, $f = f_1$. The experimental and simulation results (marked by solid red dot and blue square, respectively) are in good agreement. In addition, we observe that V_∞ can also be anticipated with the use of the **H**–field amplitude at the origin of the ME receiver instead of $\langle H_0 \rangle$, while not compromising the accuracy of the theoretical model. In this case, we assume that the **H**–field is distributed uniformly over the volume of the beam. This finding is explained by the fact that the size of the receiver is relatively small compared to that of the transmitter. Hence, the applied **H**–field varies almost linearly from one end to the other end of the ME

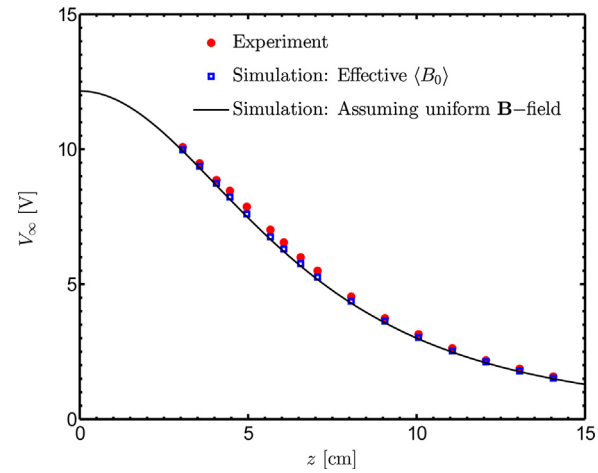

Fig. 6. Effects of non-uniform magnetic field on the open-circuit voltage along the z direction. Note, $\langle B_0 \rangle = \mu_0 \langle H_0 \rangle$.

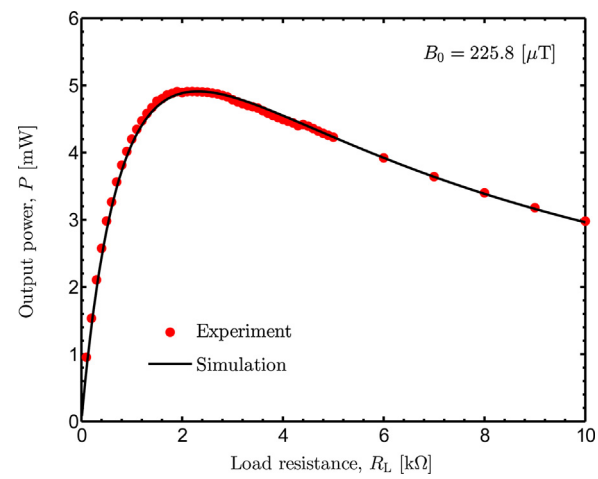

Fig. 7. Output power with respect to load resistance: Comparison between experimental data and simulation results. The drive frequency is kept fixed at the anti-resonance frequency $f = f_1 = 70.47$ kHz, for all measurements.

laminate, which allows us to approximate $\langle H_0 \rangle$ by the value of H_0 taken at the beam center. This statement may not hold in general. However, it is applicable to a smaller receiver (e.g., which is in a dimension of mm or μm) with the same or similar transmitter used.

It is important to note that α_{ME} is only a function of the constitutive material properties and the operating frequency. Therefore, α_{ME} achieves the value of 41.17 Vcm^{-1}Oe^{-1} and is unchanged for all V_∞ seen in Figure 6.

3.3. Transferred power

The most important goals of the paper are to validate equation (13) and to assess the maximum power transferred of the ME WPTS under the effects of the field non-uniformity, misalignment, and misorientation. These concerns are to be addressed in this section.

Following the principle of impedance matching to optimize the delivered power, the load resistance is varied to experimentally determine its optimum, as shown in Figure 7. The drive frequency is set at the anti-resonance frequency f_1. Under a **B**–field amplitude of $B_0 = 225.8$ μT, a maximum output power of max$\{P\} = 4.91$ mW is attained with the optimal load of $R_{L-opt} = 2.2$ kΩ. The difference between the experimental and predicted data is negligibly small. For a low coupling between the magnetic and mechanical domains, R_{L-opt} is isolated from the impedance of the thick coil.

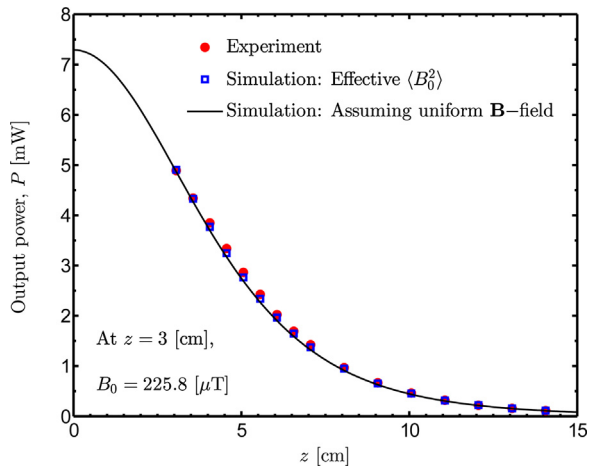

Fig. 8. Effects of non-uniform magnetic field on the power delivered to the load in the z−axis. Conversion: $\langle B_0^2 \rangle = \mu_0 \langle H_0^2 \rangle$.

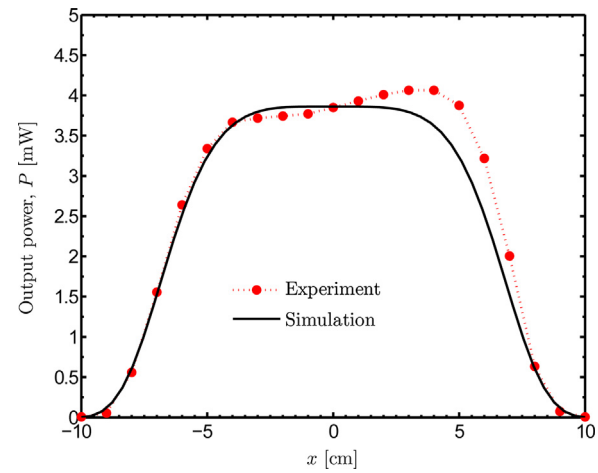

Fig. 9. Effects of alignment on the output power with respect to the lateral position (x−axis). The distance between the transmitter and receiver centers is $z = 4$ cm. The **B**–field amplitude at $x = 0$ cm is $B_0 = 197.2$ μT.

Meanwhile, f_1 is only dependent on the natural mechanical characteristics of the laminate and the electromechanical coupling. The pair of $(f_1,\ R_{\mathrm{L-opt}})$ is unchanged against the receiver location or the applied magnetic field, which is hence utilized for the remaining investigations on the performance of the ME WPTS in this Section.

Figure 8 shows the responses of the output power to the decrease of the applied **B**-field when moving the ME generator away from the transmit coil. Similar to estimating $\langle H_0 \rangle$, the effective **H**–field amplitude squared $\langle H_0^2 \rangle$ (or $\langle B_0^2 \rangle$, equivalently) is computed from equations (14) and (18) with $N = 2000$. The characteristics inferred from analyzing V_∞ in Figure 6 still hold true and are applicable to the transferred power P; in which using H_0^2 acquired at the ME transducer center (with an assumption of uniform magnetic field distribution inside the magnetostrictive material) is sufficient to describe the dynamics of P. The simulation results in both cases follow closely with those of measurements. In a general trend, the received power decreases faster at a distance range that is closer to the transmitter; it is coincident with the property of the **B**–field produced by the thick coil. At $z = 3$ cm, $P = 4.89$ mW, and when z equals to the diameter of the transmit antenna, $z \approx 15$ cm, P drops to nearly zero.

In order to quantify the influence of the alignment between the transmitter centerline and the longitudinal axis of the ME laminate to the behavior of the generated power, we adjust the location of the receiver only in the x–direction ($y = 0$) while keeping it at a fixed distance of $z = 4$ cm from the coil origin. The experimental and simulation data for $x \in [-10,\ 10]$ cm are compared in Figure 9, which, overall, are in good agreement. The discrepancy observed in the right-hand side of the figure could be due to the imperfect symmetry of the coil that might occur during the winding process. Despite that, the model is still able to capture the main essence of the considered system. Note that, at $x = 0$, the corresponding power is $P_{x_0} = 3.85$ mW, which is identical to that measured at the same gap of $z = 4$ cm in Figure 8. There is a certain range of the misalignment, $x \in \mathbb{X} = [-x_c,\ x_c]$, such that $P/P_{x_0} \geq 90\,\%$. The specific value of x_c depends on z. The set $\mathbb{X}$ is broader at smaller z and becomes narrower with an increase of z. In the case of $z = 4$ cm, $x_c/r_c \approx 1/2$ where r_c is the coil radius and $r_c = (r_1 + r_2)/2$. Comparing the whole span of $\mathbb{X}$ to the width of the laminate, we get a ratio of $2x_c/w \approx 8$, which means the receiver can be located in a space that is much bigger than its size without losing any significant power. However, outside this region, P is sensitive to the alignment error and reduces substantially with only a small further increase of $|x|$.

Figure 10 shows an experimental setup for evaluating the effects of the orientation angle θ on the output power P, in which the ME receiver is rotated about the global coordinate x at its origin O_t. An experimental example with $\theta = 20^\circ$ is depicted. The relative locations of the two permanent magnets and the laminated composite are fixed, such that the DC bias field strength is kept unchanged during the measurement.

Let us consider a magnetic field vector that is oriented with the z–axis, H_z. The effective **H**–field acting on the magnetostrictive material, which is a projection of H_z onto the length direction of the transducer, is given by

$$H_\theta = H_z \cos\theta. \tag{16}$$

Denoting the power delivered to the load at the nominal position (i.e., $\theta = 0$) as P_0, based on equations (13) and (16), the generated power for an arbitrary angle can be written as

$$P_\theta = P_0(\cos\theta)^2. \tag{17}$$

It is apparent that, $P_\theta \to P_0$ as $\theta \to 0$ and $P_\theta \to 0$ if $\theta \to \pi/2$ (or 90° equivalently). The accuracy of the prediction by (17) is presented in Figure 11, in which the measured and simulated data are nearly identical for all $\theta \in [0,\ \pi/2]$. In this case, the nominal power is $P_0 = 4.89$ mW, attained at $z = 3$ cm. Since the ratio P_θ/P_0 is only dependent on θ, and not z, equation (17) is simple but efficient to anticipate the behavior of the induced power with respect to the misorientation angle.

4. Discussion

As the validity of the complete system model has been demonstrated in previous sections, we proceed with further analysis. The direct influence of the transmitter geometry and configuration on the generated power are of interest. In particular, attempts to reduce the effects of the field non-uniformity and the misorientation are theoretically considered.

$$H_z(r,\ z) = \frac{\mathbf{J}}{4\pi} \int_{r_1}^{r_2} \int_{\varphi_1}^{\varphi_2} \int_{z_1}^{z_2} \frac{(\tilde{r} - r\cos\tilde{\varphi})\tilde{r}}{\left(r^2 + \tilde{r}^2 - 2r\tilde{r}\cos\tilde{\varphi} + (z - \tilde{z})^2\right)^{3/2}} \mathrm{d}\tilde{r}\mathrm{d}\tilde{\varphi}\mathrm{d}\tilde{z}$$

$$\text{where } \mathbf{J} = \frac{\mathbf{I}}{(z_2 - z_1)(r_2 - r_1)}. \tag{18}$$

Figure 12 shows the change of the power delivered to the load along the transmitter center axis, $(x,\ y,\ z) = (0,\ 0,\ z)$, with different radii of the transmitting coil, $r_c/2$, r_c and $2r_c$ where r_c is the nominal radius of the coil currently in use in experiments. For this comparison, the (effective) input current **I** is altered accordingly

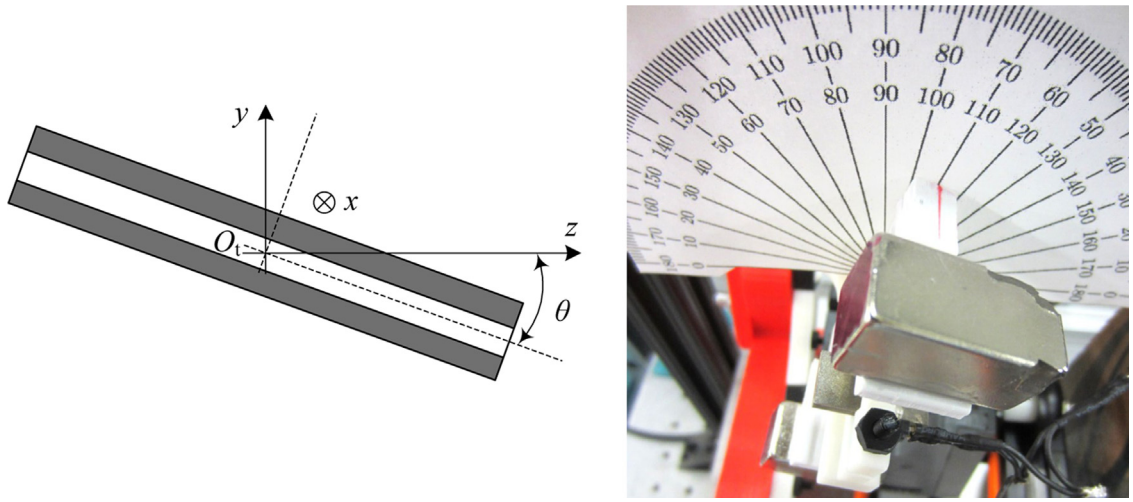

Fig. 10. Experimental setup used for investigating the effects of the orientation between the longitudinal direction of the ME transducer and the centerline of the transmit coil. The ME laminate is rotated about the x−axis while O_t is kept fixed.

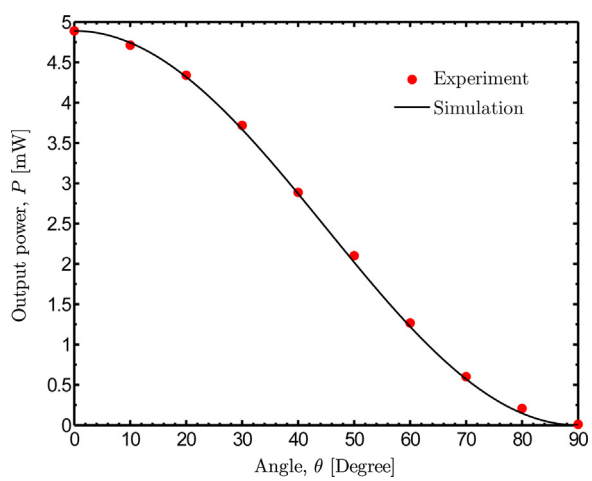

Fig. 11. Effects of the orientation of the receiver to the transmitter on the output power. The transmitter-to-receiver distance is $z = 3$ cm. At $\theta = 0$, the **B**–field amplitude is $B_0 = 225.8$ μT.

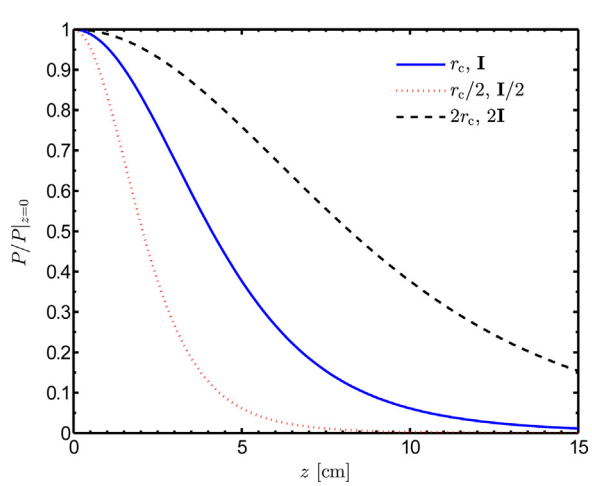

Fig. 12. Effects of coil radius on the power delivered to the load with respect to the transfer distance z, assuming perfect alignment and orientation, $x = y = 0$, $\theta = 0$. $P|_{z=0}$ are identical for all three cases, and $r_c = (r_1 + r_2)/2 = 8.07$ cm.

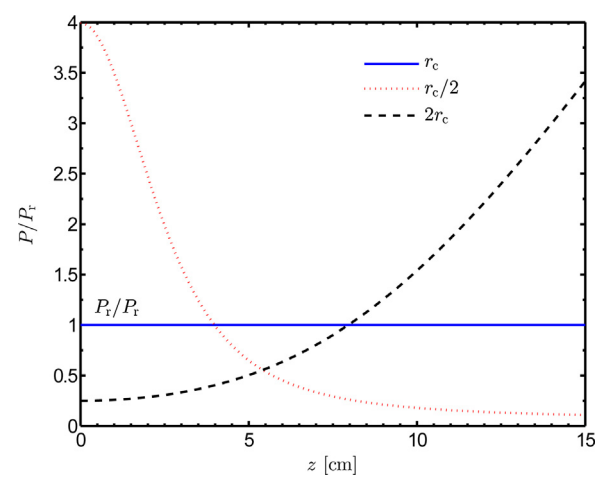

Fig. 13. Comparison of transferred power for different coil radii with the same arbitrary input current, characterized by the ratio P/P_r where P_r is the output power of the current coil design used as a reference power. $r_c = (r_1 + r_2)/2 = 8.07$ cm, and P_r is also a function of z.

to keep the **B**–field strength produced at $z = 0$ identical. In general, the transferred power drops faster with smaller coils as the transfer distance increases. However, bigger coil requires higher **I** to generate the same $B_0|_{z=0}$, and the change (increase or decrease) of **I** is proportional to that of the radius. For instance, doubling r_c leads to a doubling of **I**. Therefore, a trade-off between the coil size and input current needs to be balanced in an effort of minimizing the effects of the field non-uniformity on the output power P.

In another perspective, we now consider the behavior of P with respect to z when the input current **I** is set to be equal at an arbitrary value, regardless of the coil radius. The obtained results are shown in Figure 13 for three coil radii, in which the power corresponding to the current design of the transmitter is chosen as a reference, P_r. In order to maximize the power transferred to the load, the choice of the coil diameter depends upon the transfer distance. At close range, a smaller coil is more suitable with higher power generated. However, a bigger coil is preferable for a larger transfer range. This universal tendency is less apparent in a RIC WPTS when a small coil may not give any benefit to the received power at a short separation [24].

Figure 14 presents the simultaneous influences of the transfer distance and the orientation angle on the delivered power,

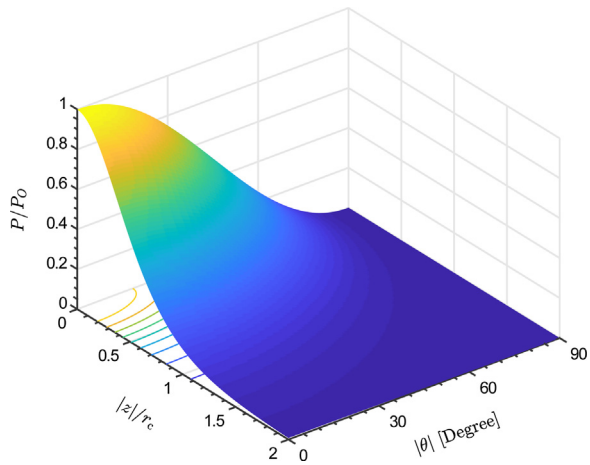

Fig. 14. Combined influences of both the transfer distance and orientation on the actual power delivered to the load, characterized by the ratio P/P_O where $P_O = P|_{x=y=z=0,\,\theta=0}$ is the power obtained at the transmitter origin O without any misorientation.

expressed by $|\theta|$ and two normalized parameters P/P_O and $|z|/r_c$, where the reference power and coil radius are $P_O = P|_{x=y=z=0,\,\theta=0}$ and $r_c = (r_1 + r_2)/2 = 8.07$ cm, respectively. The input current, **I**, is the same as used for Figure 8. As an apparent trend, any increase of either $|z|$ or $|\theta| \in [0, \pi/2]$ results in a significant drop of the output power. The combined effects even lead to a faster decrease of P. Moreover, the contours (also known as level sets) in the $z - \theta$ plane show that there exist different positions of the ME receiver yielding the same power.

Due to the characteristic shown in (17), a possible configuration to reduce the effects of misorientation is to utilize two transmitting coils electrically connected in series such that their center lines are perpendicular to each other and approximately intersect at the location of the receiver. Under this circumstance, only one input current **I** is required for operation, and the obtained power becomes $P_\theta = P_0\cos^2(\theta) + P_0'\cos^2(\pi/2 - \theta) = P_0\cos^2(\theta) + P_0'\sin^2(\theta)$, where P_0 and P_0' are the nominal power at zero-distance corresponding to the two transmitters ($z = 0$ and $z' = 0$). Especially, if $z \approx z'$, $P_0 \approx P_0'$, and as a consequence, $P_\theta \approx P_0$. However, the power losses increase due to the series parasitic resistance of the second inductor, which might lead to a decrease in the transfer efficiency. If the two coils are identical, the total power dissipated in the stray resistances is double that of when using one single transmitter. It should be noted that the efficiency of a ME WPTS is rather low, ~0.12 % as reported in [21]. However, for many low-power systems such as wireless sensor networks, efficiency may not be the key factor of interest, but the actual delivered power instead.

The maximum possible received power is bounded by the power input to the mechanical domain, and is determined by $P_{avt} = F_0^2/(8b)$, where F_0 is a product of the magnetic field amplitude H_0 and the electrodynamic transduction factor Γ_m. For a given distance z and input current **I**, H_0 is merely dependent on the dimension of the transmitting coil, and Γ_m is only a function of the geometry and material properties of the magnetostrictive phase. Thus, F_0 (and accordingly, P_{avt}) can be maximized by optimizing the transmitter and the receiver independently. On the contrary, the magnetic induction between two coils of a RIC WPTS is modeled by a mutual inductance M that simultaneously depends on both coil geometries [25]. Therefore, this approach is more challenging to apply for RIC architecture. Furthermore, while the conventional receiver antenna relies on the electromagnetic wavelength, a ME antenna

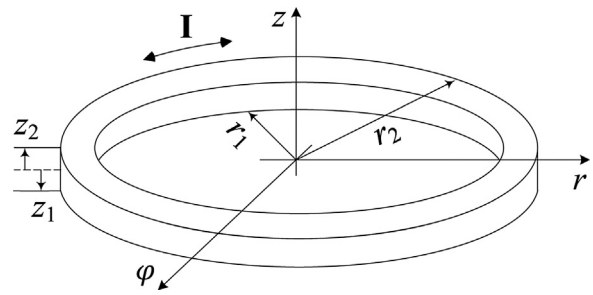

Fig. 15. Geometry of a thick coil carrying a uniform current density. Here, **I** is the current flowing in the coil.

is not limited by the size of an electromagnetic wave. It hence can be much smaller than the state-of-the-art antenna designs [26]. This critical fact could lead to dramatic miniaturization of the implanted receiver. As a ME WPTS usually operates at a low-frequency range ($\ll$ 1 MHz), the human body is nearly transparent to the applied magnetic field [27]. The energy absorbed by the tissues and the frequency shift phenomenon are negligible. All these advantages make the ME transducer a promising alternative solution to the RIC WPTS and pave a new way for powering biomedical devices.

Subject to the IEEE safety standards [10,11], at 70.47 kHz the largest allowable amplitude of the **B**–field that can be applied to humans is 205 μT. With the same operating frequency and maximum magnetic field strength, the system under investigation is able to transfer up to 4.16 mW to a load resistance (which is equivalent to 3.85 mW with 197.2 μT as shown in Figure 9). This amount of power is sufficient to supply most of the biosensors. These observations further enhance the potential use of a ME WPTS in biomedical applications.

5. Conclusions

We have investigated how the non-uniformity of the applied magnetic field, and the misalignment/misorientation between the transmitter and receiver, affect the maximum power transferred to the load. The analytical models for both transmitting and receiving sides presented in this work were proven to be sufficiently and consistently accurate to capture the fundamental dynamics of the ME WPTS under consideration. The spatial distribution of the magnetic field generated by the transmit coil is the most important factor, as it determines the capability of the power transmission for a given ME transducer. The output power is more sensitive to the change of the orthogonal distance from the ME laminate origin to the coil plane than to the variation of the alignment in parallel with the coil diameter. We also found that the delivered power is proportional to the squared cosine of the orientation angle. The findings were validated by different sets of experiments.

For small-scale ME transducers used in implantable biomedical applications, as long as the effective **B**–field at the receiver location is maximized (subject to some safety constraints), the field uniformity is not essentially required.

Author statement

Binh Duc Truong and Shad Roundy conceptualized the project; Erik Andersen and Curtis Casados designed and implemented the transmitter; Binh Duc Truong developed the theoretical model, performed experiments and simulations, and analyzed results; Binh Duc Truong and Shad Roundy wrote the manuscript.

Conflict of interests

The authors declare that there is no conflict of interests regarding the publication of this article.

Declaration of Competing Interest

The authors report no declarations of interest.

Acknowledgments

This material is based upon work supported by the National Science Foundation under Grant Number ECCS-1651438. The authors would like to thank website https://www.kindpng.com/ for providing an open-source image used in the Graphical Abstract.

Appendix A. Magnetic field produced by a thick coil with rectangular cross section [23]

Figure 15 shows the geometric dimensions of a thick coil that carries a uniform current density **J**. In particular, r_1 and r_2 are the inner and outer radii, z_1 and z_2 are the lower and upper heights. Usually, $z_1 = -z_2 = t_c/2$ where t_c is the total thickness of the coil. Without losing the generality, the cylindrical coordinates are used to describe the magnetic field in the z–direction, denoted as $H_z(r, z)$, which is of our interest in this paper. Another formulation with the Cartesian coordinate system was presented in [22]. Both approaches give the same results, thus which formulation to choose is a matter of convenience, not of physics. The role of the r–axis is now the same as that of x– or y–coordinate in Figure 1. The analytical solution of $H_z(r, z)$ is expressed in equation (18), where $\tilde{r}$, $\tilde{\varphi}$ and $\tilde{z}$ are the integration variables, $\varphi_1 = 0$ and $\varphi_2 = 2\pi$. This three-dimensional integral can be numerically computed by the function [*integral3*] in MATLAB.

References

[1] D.-H. Kim, N. Lu, R. Ma, Y.-S. Kim, R.-H. Kim, S. Wang, J. Wu, S.M. Won, H. Tao, A. Islam, K.J. Yu, T.-i. Kim, R. Chowdhury, M. Ying, L. Xu, M. Li, H.-J. Chung, H. Keum, M. McCormick, P. Liu, Y.-W. Zhang, F.G. Omenetto, Y. Huang, T. Coleman, J.A. Rogers, Epidermal electronics, Science 333 (6044) (2011) 838–843.
[2] S.M.R. Islam, D. Kwak, M.H. Kabir, M. Hossain, K. Kwak, The internet of things for health care: a comprehensive survey, IEEE Access 3 (2015) 678–708.
[3] S. Furman, J.B. Schwedel, An intracardiac pacemaker for Stokes-Adams seizures, N. Engl. J. Med. 261 (19) (1959) 943–948, PMID: 13825713.
[4] R. Bashirullah, Wireless implants, IEEE Microwave Mag. 11 (2010) S14–S23.
[5] M. Song, P. Belov, P. Kapitanova, Wireless power transfer inspired by the modern trends in electromagnetic, Appl. Phys. Rev. 4 (2) (2017) 021102.
[6] K. Agarwal, R. Jegadeesan, Y. Guo, N.V. Thakor, Wireless power transfer strategies for implantable bioelectronics, IEEE Rev. Biomed. Eng. 10 (2017) 136–161.
[7] H. Kim, H. Hirayama, S. Kim, K.J. Han, R. Zhang, J. Choi, Review of near-field wireless power and communication for biomedical applications, IEEE Access 5 (2017) 21264–21285.
[8] Z. Zhang, H. Pang, A. Georgiadis, C. Cecati, Wireless power transfer—an overview, IEEE Trans. Ind. Electron. 66 (2019) 1044–1058.
[9] A.I. Al-Kalbani, M.R. Yuce, J. Redouté, A biosafety comparison between capacitive and inductive coupling in biomedical implants, IEEE Antennas Wirel. Propag. Lett. 13 (2014) 1168–1171.
[10] IEEE, IEEE standard for safety levels with respect to human exposure to electromagnetic fields, 0–3 kHz, IEEE Std C95.6-2002, 2002, pp. 1-0.
[11] IEEE, IEEE standard for safety levels with respect to human exposure to radio frequency electromagnetic fields, 3 kHz to 300 GHz, IEEE Std C95.1-2005 (Revision of IEEE Std C95.1-1991), 2006, pp. 1–238.
[12] International Commission on Non-Ionizing Radiation Protection, Guidelines for limiting exposure to time-varying electric, magnetic, and electromagnetic fields (up to 300 GHz), Health Phys. 75 (1998).
[13] International Commission on Non-Ionizing Radiation Protection, Guidelines for limiting exposure to time-varying electric and magnetic fields (1 Hz to 100 kHz), Health Phys. 99 (2010).
[14] M. Manteghi, A.A.Y. Ibraheem, On the study of the near-fields of electric and magnetic small antennas in lossy media, IEEE Trans. Antennas Propag. 62 (2014) 6491–6495.
[15] A. Kurs, A. Karalis, R. Moffatt, J.D. Joannopoulos, P. Fisher, M. Soljacic, Wireless power transfer via strongly coupled magnetic resonances, Science 317 (2007).
[16] A.P. Sample, D.T. Meyer, J.R. Smith, Analysis, experimental results, and range adaptation of magnetically coupled resonators for wireless power transfer, IEEE Trans. Ind. Electron. 58 (2011) 544–554.
[17] V.R. Challa, J.O. Mur-Miranda, D.P. Arnold, Wireless power transmission to an electromechanical receiver using low-frequency magnetic fields, Smart Mater. Struct. 21 (11) (2012) 115017.
[18] B.D. Truong, S. Williams, S. Roundy, Experimentally validated model and analytical investigations on power optimization for piezoelectric-based wireless power transfer systems, J. Intell. Mater. Syst. Struct. 30 (16) (2019) 2464–2477.
[19] H. Basaeri, Y. Yu, D. Young, S. Roundy, Acoustic power transfer for biomedical implants using piezoelectric receivers: effects of misalignment and misorientation, J. Micromech. Microeng. 29 (2019) 084004.
[20] G. Ke, Q. Chen, W. Gao, S. Wong, C.K. Tse, Z. Zhang, Research on IPT resonant converters with high misalignment tolerance using multicoil receiver set, IEEE Trans. Power Electron. 35 (2020) 3697–3712.
[21] B.D. Truong, S. Roundy, Experimentally validated model and power optimization of a magnetoelectric wireless power transfer system in free-free configuration, Smart Mater. Struct. (2020).
[22] S. Babic, Z. Andjelic, B. Krstajic, S. Salon, Analytical calculation of the 3d magnetostatic field of a toroidal conductor with rectangular cross section, IEEE Trans. Magn. 24 (1988) 3162–3164.
[23] R. Ravaud, G. Lemarquand, V. Lemarquand, S. Babic, C. Akyel, Calculation of the magnetic field created by a thick coil, J. Electromagn. Waves Appl. 24 (10) (2010) 1405–1418.
[24] B.H. Waters, B.J. Mahoney, G. Lee, J.R. Smith, Optimal coil size ratios for wireless power transfer applications, in, 2014 IEEE International Symposium on Circuits and Systems (ISCAS) (2014) 2045–2048.
[25] S. Raju, R. Wu, M. Chan, C.P. Yue, Modeling of mutual coupling between planar inductors in wireless power applications, IEEE Trans. Power Electron. 29 (2014) 481–490.
[26] T. Nan, H. Lin, Y. Gao, A. Matyushov, G. Yu, H. Chen, N. Sun, S. Wei, Z. Wang, M. Li, X. Wang, A. Belkessam, R. Guo, B. Chen, J. Zhou, Z. Qian, Y. Hui, M. Rinaldi, M.E. McConney, B.M. Howe, Z. Hu, J.G. Jones, G.J. Brown, N.X. Sun, Acoustically actuated ultra-compact NEMS magnetoelectric antennas, Nat. Commun. 8 (2017).
[27] K.L. Kaiser, Electromagnetic shielding, CRC/Taylor and Francis, Boca Raton, London, 2006, This material was previously published in The Electromagnetic Compatibility Handbook, CRC Press, 2004.

Biographies

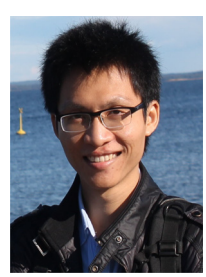

Binh Duc Truong received the B.E. degree in Mechatronics from the Ho Chi Minh City University of Technology, Vietnam, in 2012 and the M.Sc. degree in Micro- and Nano System Technology from the Buskerud and Vestfold University College, Norway, in 2015. He is currently pursuing the Ph.D. degree with Department of Mechanical Engineering, University of Utah, focusing on energy harvesting and wireless power transfer systems.

Erik Andersen received his Bachelor of Science and Masters of Mechanical Engineering from the University of Utah in 2018. He is currently a Ph.D. candidate under Dr. Shad Roundy at the University of Utah, Salt Lake City, Utah. His research interests include wireless power transfer (specifically for implantable biomedical devices), system design and optimization, and magnetoelectric transducers.

Curtis Casados received his Bachelor of Science in Mechanical Engineering from the University of Utah in 2020 and is continuing his Masters of Computer Science at the University of Southern California. He assisted in Dr. Shad Roundy's lab at the University of Utah, Salt Lake City, Utah. His research interests include wireless power transfer as well as energy harvesting.

Shad Roundy received the M.S. and Ph.D. degrees in mechanical engineering from the University of California, Berkeley, Berkeley, CA, USA in 2000 and 2003, respectively. He joined the faculty at the University of Utah in 2012 where he is currently an Associate Professor in the Department of Mechanical Engineering. From 2005 to 2012 he worked in the MEMS industry developing tire pressure sensors, accelerometers, gyroscopes, and energy harvesters. From 2003 to 2005 he was a Senior Lecturer at the Australian National University. His research interests include energy harvesting, wireless power transfer, and more generally MEMS sensors and actuators.